Structural Analysis of Wind-Turbine Blades by a Generalized Timoshenko Beam Model

Alejandro D. Otero[1]
e-mail: adotero@mtu.edu

Fernando L. Ponta[2]
e-mail: flponta@mtu.edu

Department of Mechanical Engineering-Engineering Mechanics,
Michigan Technological University,
1400 Townsend Drive,
Houghton, MI 49931

An important aspect in wind-turbine technology nowadays is to reduce the uncertainties related to blade dynamics by the improvement of the quality of numerical simulations of the fluid-structure interaction process. A fundamental step in that direction is the implementation of structural models capable of capturing the complex features of innovative prototype blades, so that they can be tested at realistic full-scale conditions with a reasonable computational cost. To this end, we developed a code based on a modified implementation of the variational-asymptotic beam sectional (VABS) technique proposed by Hodges et al. VABS has the capacity of reducing the geometrical complexity of the blade section into a stiffness matrix for an equivalent beam, allowing accurate modeling of the 3D structure of the blade as a 1D finite-element problem. In this paper, we report some recent results we have obtained by applying our code to full-scale composite laminate wind-turbine blades, analyzing the fundamental vibrational modes and the stress load in normal operational conditions. [DOI: 10.1115/1.4000596]

1 Introduction

During the last two decades, there has been a spontaneous tendency in the wind-turbine industry to increase the size of the state-of-the-art machine. This tendency is driven by economies-of-scale factors that substantially reduce the cost of wind energy. Output power of the state-of-the-art wind turbines nowadays is in the range of 3.6–6 MW, with rotor diameters of up to 127 m. Commercial models within this range are available from several manufacturers such as GE, RE-Power, Enercon, Vestas, and Siemens. The technological challenge in wind power nowadays is to develop the next generation of feasible upscaled turbines of cheaper construction that may further reduce generation costs. Now, industry insiders are talking about next-generation offshore turbine giants of 7.5–12 MW with rotor diameters of up to 200 m [1]. If this generation of superturbines is successfully developed, wind-energy costs would be reduced substantially.

Hence, an important aspect in wind-turbine technology nowadays is to reduce the uncertainties related to blade dynamics, by the improvement of the quality of numerical simulations of the fluid-structure interaction process, and by a better understanding of the underlying physics. The goal is to provide the industry with a tool that helps them to introduce new technological solutions to improve the economics of blade design, manufacturing, and transport logistics, without compromising reliability. The current state-of-the-art is to solve the aeroelastic equations in a fully nonlinear coupled mode using Bernoulli or Timoshenko beam models (see Ref. [2], where a thorough coverage of the topic is presented). Further step in that direction is the implementation of structural models capable of capturing the complex features of innovative prototype blades, so they can be tested at realistic full-scale conditions with a reasonable computational cost. To this end, we developed a code based on a modified implementation—the variational-asymptotic beam sectional (VABS) technique proposed by Hodges et al. [3,4]. In this paper we report some recent results we have obtained applying our code to full-scale composite laminate wind-turbine blades, analyzing the fundamental vibrational modes and the stress load in normal operational conditions.

2 Theoretical Basis of VABS and 1D Beam Model

Even though a blade is a slender structure that may be studied as a beam, they are usually not simple to model due to the inhomogeneous distribution of material properties and the complexity of their cross section (see Fig. 1). The ad hoc kinematic assumptions made in classical theories (such as the Bernoulli or the standard Timoshenko approaches) may introduce significant errors, especially when the blade is vibrating with a wavelength shorter than its length. In order to obtain an advance model capable of dealing with the complex features of new-generation blades, we developed a code based on a modified implementation of the VABS model. Proposed and developed by Professor Hodges and his collaborators [3–7], VABS is a model for curved and twisted composite beams that uses the same variables as the classical Timoshenko beam theory, but the hypothesis of beam sections remaining planar after deformation is abandoned. Instead, the real warping of the deformed section is interpolated by a 2D finite-element mesh and its contribution to the strain energy is put in terms of the classical 1D Timoshenko's variables by means of a preresolution. The geometrical complexity of the blade section and/or its material inhomogeneousness are reduced into a stiffness matrix for the 1D beam. The reduced 1D strain energy is equivalent to the actual 3D strain energy in an asymptotic sense. Elimination of the ad hoc kinematic assumptions produces a fully populated 6×6 symmetric matrix for the 1D beam, with as many as 21 stiffnesses, instead of the six fundamental stiffnesses of the original Timoshenko theory [8]. That is why VABS is referred to as a *generalized Timoshenko theory*.

Even for the case of large displacements and rotations of the beam sections, VABS allows for accurate modeling of the bending and transverse shear in two directions, extension, and torsion of the blade structure as a 1D finite-element problem. Thus, through VABS we are able to decouple a general 3D nonlinear anisotropic elasticity problem into a linear, 2D, cross-sectional analysis (that may be solved a priori), and a nonlinear, 1D beam analysis for the

[1]Present address: College of Engineering, University of Buenos Aires.
[2]Corresponding author.

Contributed by the Solar Energy Division of ASME for publication in the JOURNAL OF SOLAR ENERGY ENGINEERING. Manuscript received December 23, 2008; final manuscript rceived November 6, 2009; published online January 5, 2010. Assoc. Editor: Spyros Voutsinas.

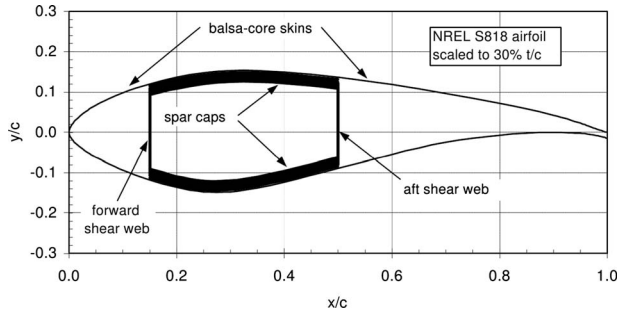

Fig. 1 Example of blade-section structural architecture representative of current commercial blade designs. The primary structural member is a box-spar, with a substantial buildup of spar cap material between the webs. The exterior skins and internal shear webs are both sandwich constructions with triaxial fiberglass laminates separated by balsa core (from Ref. [23]).

global problem, which is needed at each time step of a fluid-structure interaction analysis. This reduces the computational cost with respect to a 2D shell or a full 3D solid model as the structural problem is solved along many timesteps. The cross-sectional 2D analysis (that may be performed in parallel for all the cross sections along the blade) calculates the 3D warping functions asymptotically and finds the constitutive model for the 1D nonlinear beam analysis of the blade. After one obtains the global deformation from the 1D beam analysis, the original 3D fields (displacements, stresses, and strains) can be recovered a posteriori using the already-calculated 3D warping functions.

Detailed descriptions of the development of VABS can be found in Refs. [4,5,7–11], including validation tests for different cases of complex beams, and applications to helicopter and wind-turbine blades. In order to make this paper selfcontained, a brief outline of VABS theoretical basis is given. Referring to Fig. 2, the beam is represented by a reference line R in the undeformed configuration, which could be twisted and/or curved. At every point along R, an associated orthogonal triad—$\underline{\mathbf{B}}_1$, $\underline{\mathbf{B}}_2$, and $\underline{\mathbf{B}}_3$—is defined in such a way that $\underline{\mathbf{B}}_1$ is tangent to R, and $\underline{\mathbf{B}}_2$ and $\underline{\mathbf{B}}_3$ are contained into the section plane, which is normal to R. A correspondent coordinate system (X^1, X^2, X^3) is defined, where X^1 is the coordinate along R, and X^2 and X^3 are the Cartesian coordinates on the section plane. When the structure is deformed due to loading, the original reference line R adopts a new geometry r, and we have a new triad—$\underline{\mathbf{t}}_1$, $\underline{\mathbf{t}}_2$, and $\underline{\mathbf{t}}_3$—associated to each point, where $\underline{\mathbf{t}}_1$ is tangent to r, and $\underline{\mathbf{t}}_2$ and $\underline{\mathbf{t}}_3$ are contained into the

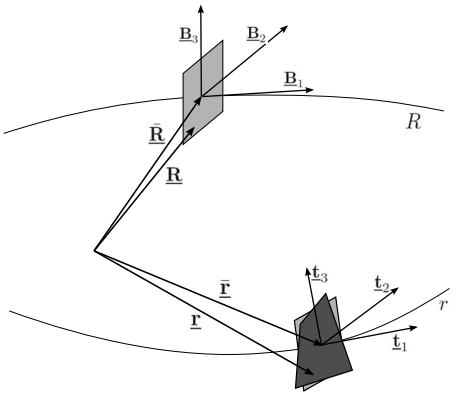

Fig. 2 VABS model: schematic of the reference line, orthogonal triads, and beam sections before and after deformation (after Ref. [4])

normal plane. The position of a generic point on each section in the underformed configuration may be written as

$$\underline{\mathbf{R}}(X^i) = \bar{\underline{\mathbf{R}}}(X^1) + X^\alpha \underline{\mathbf{B}}_\alpha(X^1) \underline{\mathbf{R}} \tag{1}$$

where $\underline{\mathbf{R}}$ denotes the position of the center of the tern along R, and the index α assumes the values 2 and 3. The material point whose original position was given by $\underline{\mathbf{R}}(X^i)$ has, after the deformation, the position vector

$$\underline{\mathbf{r}}(X^i) = \bar{\underline{\mathbf{R}}} + \underline{\mathbf{u}} + X^\alpha \underline{\mathbf{t}}_\alpha + w_i \underline{\mathbf{t}}_i \tag{2}$$

where w_i are the contribution to the displacement due to warping. Now, we are able to compute for the components of the gradient-of-deformation tensor as $F_{ij} = \underline{\mathbf{t}}_i \cdot \underline{\mathbf{g}}_k \underline{\mathbf{G}}^k \cdot \underline{\mathbf{B}}_j$, where $\underline{\mathbf{g}}_k$ and $\underline{\mathbf{G}}^k$ are the covariant base vectors for the deformed configuration and the contravariant base vectors in the undeformed configuration, obtained from the kinematic description of Eqs. (1) and (2), respectively. The Jaumann–Biot–Cauchy strain tensor is $\Gamma_{ij} = 1/2(F_{ij} + F_{ji}) - \delta_{ij}$, which provides a suitable measure of the 3D strain field in terms of the beam strain measures and arbitrary warping functions. $\boldsymbol{\Gamma}$ is then used to compute for the strain energy density function as

$$2U = \langle\langle \boldsymbol{\Gamma}^T \mathcal{S} \boldsymbol{\Gamma} \rangle\rangle \tag{3}$$

where $\mathcal{S}$ is the matrix of the characteristics of the material expressed in the $\underline{\mathbf{B}}_i$ coordinates, and $\langle\langle \bullet \rangle\rangle = \int_s \bullet \sqrt{G} dX^2 dX^3$, where s defines integration over a cross section.

The next step is to find a strain energy expression asymptotically correct up to the second order of h/l and h/R_0, where h is the characteristic size of the section, l is the characteristic wavelength of deformation along the beam axis, and R_0 is the characteristic radii of initial curvatures and twist of the beam. A complete second-order strain energy is sufficient for constructing a generalized Timoshenko model because it is generally accepted that the transverse shear strain measures are one order less than classical beam strain measures (extension, torsion, and bending in two directions) [8]. A strain energy expression that asymptotically approximates the 3D energy up to the second order is achieved using the variational-asymptotic method proposed in Ref. [12]. The complete derivation of this procedure is presented in Ref. [4], resulting in the following expression for the asymptotically correct strain energy:

$$2U = \boldsymbol{\varepsilon}^T \mathbf{A} \boldsymbol{\varepsilon} + \boldsymbol{\varepsilon}^T 2\mathbf{B} \boldsymbol{\varepsilon}' + \boldsymbol{\varepsilon}'^T \mathbf{C} \boldsymbol{\varepsilon}' + \boldsymbol{\varepsilon}^T 2\mathbf{D} \boldsymbol{\varepsilon}'' \tag{4}$$

where $\mathbf{A}$, $\mathbf{B}$, $\mathbf{C}$, and $\mathbf{D}$ are matrices that carry information on both the geometry and material properties of the cross section, $(\,)'$ indicates the partial derivative with respect to the axial coordinate X^1, and $\boldsymbol{\varepsilon} = [\bar{\gamma}_{11} \;\; \bar{\kappa}_1 \;\; \bar{\kappa}_2 \;\; \bar{\kappa}_3]^T$ are the strain measures defined in the classical Bernoulli beam theory, where $\bar{\gamma}_{11}$ is the extension of the beam reference line, $\bar{\kappa}_1$ is its torsion, and $\bar{\kappa}_2$ and $\bar{\kappa}_3$ are the bending of the reference line in axes 2 and 3 due to the deformation.

The variational-asymptotic procedure to get the matrices in Eq. (4) involves the discretization by finite-element techniques of the warping functions w_i defined in Eq. (2). To this end, four constraints are imposed on w_i. $\langle w_i \rangle = 0$ and $\langle X^2 w_3 - X^3 w_2 \rangle = 0$, where $\langle \bullet \rangle = \int_s \bullet dX^2 dX^3$ are intended to eliminate the four rigid modes of displacement of the warped section (i.e., the three linear displacements plus rotation around $\underline{\mathbf{t}}_1$), which are already included in the Bernoulli strain measures $\boldsymbol{\varepsilon}$. Previous implementations of VABS [4,7] use the technique described in Ref. [13] in order to impose these constraints. In the method of Cesnik et al., the rigid modes of displacement are suppressed explicitly. Then, the eigenvectors associated with the rigid modes in the matrix of the linear system are computed, and used in order to get a reduced system. Instead of that, herein, we use the Lagrangian-multiplier technique in its classical way to impose the constraints and solve for the expanded system for the constrained variational formulation itself. This simplifies the procedure by basically combining the whole solution in

a single step. This simplification produces by itself a certain reduction in the overall computational cost, but most importantly, it has the advantage of allowing the use of the internal-node condensation technique in the finite-element discretization. As we shall see later, internal-node condensation allows us to substantially improve the efficiency of our solution by the triquadrilateral finite-element technique.

Equation (4) for the strain energy is asymptotically correct. Nevertheless, it is difficult to be used in practice because it contains derivatives of the classical strain measures, which requires complicated boundary conditions. But the well known Timoshenko beam theory is free from such drawbacks. Hence, the next step is to fit the strain energy in Eq. (4) into a generalized Timoshenko model of the form

$$2U = \begin{bmatrix} \boldsymbol{\epsilon}^T & \boldsymbol{\gamma}_s^T \end{bmatrix} \begin{bmatrix} \mathbf{X} & \mathbf{Y} \\ \mathbf{Y}^T & \mathbf{G} \end{bmatrix} \begin{bmatrix} \boldsymbol{\epsilon} \\ \boldsymbol{\gamma}_s \end{bmatrix} = \boldsymbol{\epsilon}^T \mathbf{X} \boldsymbol{\epsilon} + 2\boldsymbol{\epsilon}^T \mathbf{Y} \boldsymbol{\gamma}_s + \boldsymbol{\gamma}_s^T \mathbf{G} \boldsymbol{\gamma}_s \tag{5}$$

where $\boldsymbol{\epsilon}=[\gamma_{11}\ \kappa_1\ \kappa_2\ \kappa_3]^T$ are the classical Timoshenko strain measures due to extension, torsion, and bending, and $\boldsymbol{\gamma}_s=[2\gamma_{12}\ 2\gamma_{13}]^T$ are the transverse shear strains.

What we need to find are **X**, **Y**, and **G** in such a way that the strain energy in Eqs. (4) and (5) would be equivalent up to at least the second order. There is an identity that relates both the Bernoulli and the Timoshenko measures of deformation

$$\boldsymbol{\varepsilon} = \boldsymbol{\epsilon} + \mathbf{Q}_\gamma \boldsymbol{\gamma}_s' + \mathbf{P}_\gamma \boldsymbol{\gamma}_s \tag{6}$$

where

$$\mathbf{Q}_\gamma{}^T = \begin{bmatrix} 0 & 0 & 0 & 1 \\ 0 & 0 & -1 & 0 \end{bmatrix}, \quad \text{y} \quad \mathbf{P}_\gamma{}^T = \begin{bmatrix} 0 & K_2 & -K_1 & 0 \\ 0 & K_3 & 0 & -K_1 \end{bmatrix} \tag{7}$$

K_1 is the twist, and K_2 and K_3 are the curvatures of the undeformed reference line R. Thus, using Eq. (6), we may rewrite Eq. (4) in terms of the generalized Timoshenko strain measures using the 1D equilibrium equations. This provides a way to relate the derivatives of strain measures with the strain measures themselves, to fit the resulting expression into the generalized Timoshenko form (Eq. (5)). Then, an asymptotic method is used to get approximations to **X**, **Y**, and **G** using as input the already computed matrices **A**, **B**, **C**, and **D** (see Ref. [4] for details). Finally, a stiffness matrix for the 1D beam problem $\bar{\mathbb{S}}$ is formed as a simple reordering of the matrix

$$\begin{bmatrix} \mathbf{X} & \mathbf{Y} \\ \mathbf{Y}^T & \mathbf{G} \end{bmatrix}$$

in such a way as to get a functional for the strain energy density of Eq. (5)

$$2U = \bar{\boldsymbol{\gamma}}^T \bar{\mathbb{S}} \bar{\boldsymbol{\gamma}} \tag{8}$$

where

$$\bar{\boldsymbol{\gamma}} = \begin{bmatrix} \boldsymbol{\gamma} \\ \boldsymbol{\kappa} \end{bmatrix}$$

is the array of Timoshenko measures of deformation regrouped in a more convenient way, $\boldsymbol{\gamma}^T=[\gamma_{11}\ 2\gamma_{12}\ 2\gamma_{13}]$, and $\boldsymbol{\kappa}^T=[\kappa_1\ \kappa_2\ \kappa_3]$.

For the discretization of the 2D sections, we adopted the triquadrilateral finite-element technique, which is based on the use of nine-node biquadratic isoparametric finite elements that possess high convergence rates and, due to their biquadratic interpolation of the geometric coordinates, provide the additional ability of reducing the so-called skin-error on curvilinear boundaries when compared with linear elements. For details, see Ref. [14].

In order to combine the advantages of the nine-node quadrilateral isoparametric element with the geometrical ability of a triangular grid to create suitable nonstructured meshes with gradual and smooth changes in mesh density, we implemented what we called the triquadrilateral isoparametric elements. The triquadrilateral elements consist of an assembly of three quadrilateral nine-node isoparametric elements, in which each triangle of a standard unstructured mesh is divided into. By static condensation of the nodes that lie inside the triangle, we can significantly reduce the number of nodes to solve in the final system, subsequently recovering the values for the internal nodes from the solution on the noncondensable nodes. The internal nodes may be expressed in terms of nodes which lay on the elemental boundary following the classical procedure for elemental condensation (see Ref. [14]). This process of condensation allows us to reduce the size of the new system to approximately 40% of the original system. The use of the static condensation procedure is attractive not only because it reduces the size of the stiffness matrices, arising in finite- and spectral-element methods but also because it improves the condition number of the final condensed system. For details, see Ref. [15].

To solve for the one-dimensional problem for the equivalent beam, we use a formulation based on the intrinsic equations for the beam obtained from variational principles [16], and weighted in an energy-consistent way according to Patil and Althoff [17], which produces the following variational formulation:

$$\int_0^\ell [\underbrace{\delta\bar{\mathbf{V}}^T \bar{\mathbb{I}} \dot{\bar{\mathbf{V}}}}_{1} + \underbrace{\delta\bar{\mathbf{F}}^T \bar{\mathbb{S}}^{-1} \dot{\bar{\mathbf{F}}}}_{2}] dX^1 = \int_0^\ell [\underbrace{\delta\bar{\mathbf{V}}^T \bar{\mathbf{F}}'}_{3} + \underbrace{\delta\bar{\mathbf{V}}^T \hat{\mathbf{K}} \bar{\mathbf{F}}}_{4} + \underbrace{\delta\bar{\mathbf{V}}^T \hat{\boldsymbol{\gamma}} \bar{\mathbf{F}}}_{5} + \underbrace{\delta\bar{\mathbf{V}}^T \bar{\mathbf{f}}}_{6} - \underbrace{\delta\bar{\mathbf{V}}^T \hat{\mathbf{V}} \bar{\mathbb{I}} \bar{\mathbf{V}}}_{7} + \underbrace{\delta\bar{\mathbf{F}}^T \bar{\mathbf{V}}'}_{8} - \underbrace{\delta\bar{\mathbf{F}}^T \hat{\mathbf{K}}^T \bar{\mathbf{V}}}_{9} - \underbrace{\delta\bar{\mathbf{F}}^T \hat{\boldsymbol{\gamma}}^T \bar{\mathbf{V}}}_{10}] dX^1 \tag{9}$$

where

$$\bar{\mathbf{F}} = \begin{bmatrix} \mathbf{F} \\ \mathbf{M} \end{bmatrix}, \quad \bar{\mathbf{V}} = \begin{bmatrix} \mathbf{V} \\ \boldsymbol{\Omega} \end{bmatrix}, \quad \bar{\mathbf{f}} = \begin{bmatrix} \mathbf{f} \\ \mathbf{m} \end{bmatrix}$$

$$\hat{\boldsymbol{\gamma}} = \begin{bmatrix} \tilde{\boldsymbol{\kappa}} & 0 \\ \tilde{\boldsymbol{\gamma}} & \tilde{\boldsymbol{\kappa}} \end{bmatrix}, \quad \hat{\mathbf{V}} = \begin{bmatrix} \tilde{\boldsymbol{\Omega}} & 0 \\ \tilde{\mathbf{V}} & \tilde{\boldsymbol{\Omega}} \end{bmatrix}, \quad \hat{\mathbf{K}} = \begin{bmatrix} \tilde{\mathbf{K}} & 0 \\ \widetilde{\mathbf{e}_1} & \tilde{\mathbf{K}} \end{bmatrix}$$

The tilde indicates the skew-symmetric matrix associated to a vector magnitude in such a way that, for example, if we have any pair of vectors **A** and **B**, the matrix-vector product $\tilde{\mathbf{A}}\mathbf{B}$ is equivalent to the cross product $\mathbf{A}\times\mathbf{B}$. Thus, $\tilde{\boldsymbol{\gamma}}$ is associated with $\boldsymbol{\gamma}$, $\tilde{\boldsymbol{\kappa}}$ with $\boldsymbol{\kappa}$, $\tilde{\mathbf{V}}$ with **V**, and so forth. Hence, matrix $\hat{\boldsymbol{\gamma}}$ is a rearrangement of the components of the strain measures vector $\bar{\boldsymbol{\gamma}}$ defined above, the generalized-velocities vector $\bar{\mathbf{V}}$ and matrix $\hat{\mathbf{V}}$ represent the components of the linear and angular velocities, and matrix $\hat{\mathbf{K}}$ represents the initial torsion and curvatures of the beam (matrix $\widetilde{\mathbf{e}_1}$ is the skew-symmetric matrix associated to $\mathbf{e}_1^T=[1\ 0\ 0]$, which is the unit vector along X^1). The generalized-forces vector $\bar{\mathbf{F}}$ represents the forces and moments related with the strain measures ($\bar{\boldsymbol{\gamma}}=\bar{\mathbb{S}}^{-1}\bar{\mathbf{F}}$) $\bar{\boldsymbol{\gamma}}=\bar{\mathbb{S}}$, and the generalized distributed loads vector $\bar{\mathbf{f}}$ represents the forces and moments distributed along the axis of the beam. Here, $\bar{\mathbb{S}}$ is the same stiffness matrix for the 1D model obtained from VABS (see Eq. (8)), and $\bar{\mathbb{I}}$ is the inertia matrix of each section. The upper dot indicates a time derivative, and the prime indicates a derivative with respect to the longitudinal coordinate of the beam X^1.

This variational formulation was discretized by the spectral-element method [18,19]. The magnitudes in Eq. (9) were replaced by their interpolated counterparts $\bar{\mathbf{V}}=\mathbf{H}_{\bar{\mathbf{V}}}^e\mathbf{Q}^e$ and $\bar{\mathbf{F}}=\mathbf{H}_{\bar{\mathbf{F}}}^e\mathbf{Q}^e$, where $\mathbf{H}_{\bar{\mathbf{V}}}^e$ and $\mathbf{H}_{\bar{\mathbf{F}}}^e$ are the interpolation-function arrays, and $\mathbf{Q}^e$ is a vector containing the nodal values of both the generalized velocities and forces. The superscript e indicates the discretization of the terms at the elemental level, which will disappear after the final

assembly of the terms into the global matrix for the whole beam. The axial derivatives of the magnitudes were interpolated in a similar way as $\bar{\mathbf{V}}' = \mathbf{B}^e_{\bar{\mathbf{V}}}\mathbf{Q}^e$, and $\bar{\mathbf{F}}' = \mathbf{B}^e_{\bar{\mathbf{F}}}\mathbf{Q}^e$, where $\mathbf{B}^e_{\bar{\mathbf{V}}}$ and $\mathbf{B}^e_{\bar{\mathbf{F}}}$ are the arrays for the interpolation-function derivatives. Then, the following discretized version of Eq. (9) is obtained as

$$\delta\mathbf{Q}^{eT}\mathbf{M}^e_{\mathbf{1}}\dot{\mathbf{Q}}^e = \delta\mathbf{Q}^{eT}(\mathbf{K}^e_{\mathbf{1}} + \mathbf{K}^e_{\mathbf{2}})\mathbf{Q}^e + \delta\mathbf{Q}^{eT}\mathbf{K}^e_{\mathbf{q}}\bar{\mathbf{q}}^e + \delta\mathbf{Q}^{eT}\mathbf{B}^e_{Q}(\mathbf{Q}^e) \tag{10}$$

where

$$\mathbf{M}^e_{\mathbf{1}} = \int_{-1}^{1} [\mathbf{H}^{eT}_{\bar{\mathbf{V}}}\bar{\mathbb{I}}\mathbf{H}^e_{\bar{\mathbf{V}}} + \mathbf{H}^{eT}_{\bar{\mathbf{F}}}\bar{\mathbb{S}}^{-1}\mathbf{H}^e_{\bar{\mathbf{F}}}]Jdt$$

$$\mathbf{K}^e_{\mathbf{1}} = \int_{-1}^{1} [\mathbf{H}^{eT}_{\bar{\mathbf{V}}}\mathbf{B}^e_{\bar{\mathbf{F}}} + \mathbf{H}^{eT}_{\bar{\mathbf{F}}}\mathbf{B}^e_{\bar{\mathbf{V}}}]Jdt\mathbf{Q}^e$$

$$\mathbf{K}^e_{\mathbf{2}} = \int_{-1}^{1} [\mathbf{H}^{eT}_{\bar{\mathbf{V}}}\hat{\mathbf{K}}\mathbf{H}^e_{\bar{\mathbf{F}}} - \mathbf{H}^{eT}_{\bar{\mathbf{F}}}\hat{\mathbf{K}}^T\mathbf{H}^e_{\bar{\mathbf{V}}}]Jdt$$

$$\mathbf{K}^e_{\mathbf{q}} = \int_{-1}^{1} \mathbf{H}^{eT}_{\bar{\mathbf{V}}}\mathbf{H}^e_{\bar{\mathbf{F}}}Jdt$$

where $\mathbf{M}^e_{\mathbf{1}}$ corresponds to the discretization of terms 1 and 2, giving the equivalent of a mass matrix, $\mathbf{K}^e_{\mathbf{1}}$, corresponding to terms 3 and 8, is the stiffness matrix of the 1D problem, $\mathbf{K}^e_{\mathbf{2}}$, corresponding to terms 4 and 9, is the additional stiffness related with the twist and curvature of the undeformed configuration, $\mathbf{K}^e_{\mathbf{q}}$ corresponds to the evaluation of term 6, which is the contribution of the distributed loads, $\bar{\mathbf{q}}^e$ is an array containing the nodal values of the generalized distributed loads, t is the natural coordinate in the elements, and J is the Jacobian of the mapping from the problem coordinate X^1 to t [14]. The discretized version of the terms in Eq. (9) related to nonlinear interactions, i.e., terms 5, 7, and 10, gives

$$\mathbf{B}^e_{Q}(\mathbf{Q}^e) = \int_{-1}^{1} [\mathbf{H}^{eT}_{\bar{\mathbf{V}}}\hat{\boldsymbol{\gamma}}\mathbf{H}^e_{\bar{\mathbf{F}}} - \mathbf{H}^{eT}_{\bar{\mathbf{V}}}\hat{\mathbf{V}}\bar{\mathbb{I}}\mathbf{H}^e_{\bar{\mathbf{V}}} - \mathbf{H}^{eT}_{\bar{\mathbf{F}}}\hat{\boldsymbol{\gamma}}^T\mathbf{H}^e_{\bar{\mathbf{V}}}]\mathbf{Q}^eJdt$$

A linearization of $\mathbf{B}^e_{Q}(\mathbf{Q}^e)$ around any given configuration $\mathbf{Q}^e_1$ gives the matrix

$$\mathbf{K}^e_{\mathbf{N}}(\mathbf{Q}^e_1) = \int_{-1}^{1} \{\mathbf{H}^{eT}_{\bar{\mathbf{V}}}[\hat{\boldsymbol{\gamma}}_1\mathbf{H}^e_{\bar{\mathbf{F}}} - \hat{\mathbf{V}}_1\bar{\mathbb{I}}\mathbf{H}^e_{\bar{\mathbf{V}}} - \hat{\mathbf{F}}_1\bar{\mathbb{S}}^{-1}\mathbf{H}^e_{\bar{\mathbf{F}}} + \hat{\mathbf{P}}_1\mathbf{H}^e_{\bar{\mathbf{V}}}] + \mathbf{H}^{eT}_{\bar{\mathbf{F}}}[\hat{\mathbf{V}}^T_1\bar{\mathbb{S}}^{-1}\mathbf{H}^e_{\bar{\mathbf{F}}} - \hat{\boldsymbol{\gamma}}^T_1\mathbf{H}^e_{\bar{\mathbf{V}}}]\}Jdt$$

where

$$\hat{\mathbf{F}} = \begin{bmatrix} \mathbf{0} & \tilde{\mathbf{F}} \\ \tilde{\mathbf{F}} & \tilde{\mathbf{M}} \end{bmatrix}, \quad \hat{\mathbf{P}} = \begin{bmatrix} \mathbf{0} & \tilde{\mathbf{P}}_v \\ \tilde{\mathbf{P}}_v & \tilde{\mathbf{P}}_\omega \end{bmatrix}$$

Matrix $\hat{\mathbf{F}}$ is a rearrangement of the components of the generalized-forces vector $\bar{\mathbf{F}}$ defined above. Matrix $\hat{\mathbf{P}}$ is a rearrangement of the components of the generalized-momentum vector

$$\bar{\mathbf{P}} = \begin{bmatrix} \mathbf{P}_v \\ \mathbf{P}_\omega \end{bmatrix}$$

which represents the linear and angular momenta related with the generalized-velocities ($\bar{\mathbf{P}} = \bar{\mathbb{I}}\bar{\mathbf{V}}$). The tilde operates in the same way defined before, and the subscript 1 indicates the value of the magnitudes at a given state $\mathbf{Q}^e_1$.

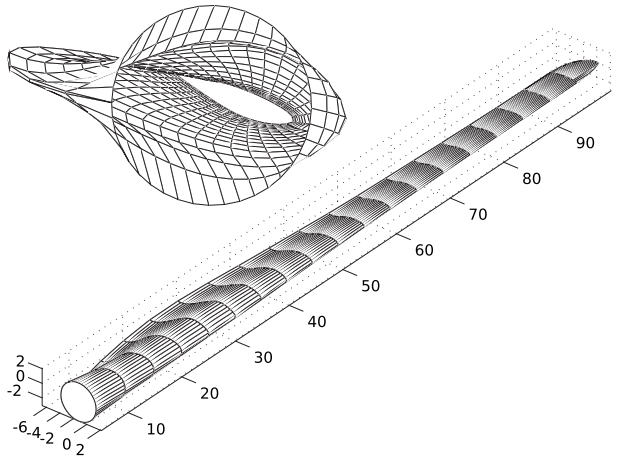

Fig. 3 A 3D view of the blade geometry

Finally, after the assembly of the elemental terms into the global system, the solution for the nonlinear problem (Eq. (9)) in its steady state was obtained by solving iteratively for the discretized expression $\boldsymbol{\Delta}\mathbf{Q}$

$$[\mathbf{K}_1 + \mathbf{K}_2 + \mathbf{K}_N(\mathbf{Q}^{(i)})]\boldsymbol{\Delta}\mathbf{Q} = -\mathbf{K}_q\bar{\mathbf{q}} - (\mathbf{K}_1 + \mathbf{K}_2)\mathbf{Q}^{(i)} - \mathbf{B}_Q(\mathbf{Q}^{(i)}) \tag{11}$$

and updating the global vector of nodal values of the generalized velocities and forces as $\mathbf{Q}^{(i+1)} = \mathbf{Q}^{(i)} + \boldsymbol{\Delta}\mathbf{Q}$.

From the steady-state solution, we also obtain the vibrational modes of the blade structure and their corresponding frequencies by solving the eigenvalue problem

$$\mathbf{M}_1\dot{\mathbf{Q}} + [\mathbf{K}_1 + \mathbf{K}_2 + \mathbf{K}_N(\mathbf{Q}^{(i)})]\mathbf{Q} = \mathbf{0} \tag{12}$$

From these results for the intrinsic equations, we recovered the displacements and rotations of the blade sections by solving the kinematic equations for the beam [20]

$$\mathbf{u}' - \mathbf{C}^T_{rR}(\boldsymbol{\gamma} + \mathbf{e}_1) + \mathbf{e}_1 + \tilde{\mathbf{K}}\mathbf{u} = \mathbf{0} \tag{13}$$

$$\tilde{\mathbf{K}} + \tilde{\boldsymbol{\kappa}} + \mathbf{C}'_{rR}\mathbf{C}^T_{rR} - \mathbf{C}_{rR}\tilde{\mathbf{K}}\mathbf{C}^T_{rR} = \mathbf{0} \tag{14}$$

where $\mathbf{u}$ is the vector of displacements of each point along the reference line from its position in the reference configuration to the one in the deformed configuration, and $\mathbf{C}_{rR}$ is the orthogonal matrix that rotates the local triad from its original orientation in the reference configuration to the one in the deformed configuration (both are defined in function of the longitudinal coordinate X^1). The strains $\boldsymbol{\gamma}$ and $\boldsymbol{\kappa}$ were computed from the generalized forces and the stiffness of the corresponding blade section. Equations (13) and (14) were also linearized and, like the other expressions, discretized by the spectral-element method.

3 Numerical Experimentation

Before applying our code to the analysis of wind-turbine blades, we had successfully validated it for different benchmark cases of complex beams. Then, we designed a 40-m long test blade using airfoil sections of the DU series. The DU series was specially developed for wind-turbine applications by researchers at Delft University, The Netherlands [21], and is currently used by the wind-turbine industry. Figure 3 shows a 3D view of the blade geometry. Six different airfoil shapes from the DU series were used in the design of the test blade. Table 1 indicates the thickness/chord length ratio for each of the airfoils used. Three thick airfoil sections were used in the inner regions of the blade at 15%, 18%, and 25% of the blade-span, where a good structural behavior is required, whereas three thin airfoils were used in the mid-span and tip regions at 45%, 60%, and 95% of the span,

Table 1 List of airfoil sections of the DU series used at each blade-span station

Position (% of blade-span)	Airfoil	Thickness (% of chord length)
15	DU 00-W2-401	40.1
18	DU 00-W2-350	35
25	DU 97-W-300	30
45	DU 91-W2-250	25
60	DU 93-W-210	21
95	DU 96/95-W-180	18

where aerodynamic efficiency is the priority. Constructive characteristics as thickness, and number and orientation of fiberglass layers for the different structural components of the blade section (see Fig. 1) were selected, following the examples included in Refs. [22,23] for blades of similar size. Each section is assumed to be composed by two aerodynamic shells, plus two spar caps which, together with two shear webs, form a box-beam spar to provide the main structural component. The aerodynamic shells are mainly composed of ± 45 deg layers, plus a small amount of randomly oriented fibers, gelcoat, and filling resin. The spar caps are composed of 0 deg layers in order to give support to the bending loads. There is a reinforcement in the rear part of the sections, i.e., the trailing edge spline, which supports the bending loads in the chordwise direction and is also made up of 0 deg fibers. The shear webs are made up of ± 45 deg layers with a core of balsa wood, which gives buckling resistance to the web. A more comprehensive description of lamination sequences and material properties can be found in Refs. [22,23].

A triquadrilateral mesh was generated for each one of these sections. Figures 4 and 5 show examples of triangulations for the sections located at 18% of the blade-span, which is a thick airfoil from the inner region, and 60% of the blade-span, which is a thin airfoil from the mid-span region respectively. A detailed view of the triquadrilateral mesh is also shown in the inset in Fig. 4. Material properties were assumed homogeneous within the subregions corresponding to each of blade-section components described above, and equal to those of an equivalent material. The properties of this equivalent material, which is a 6×6 symmetric matrix with 21 independent coefficients, were computed by a weighted average of the properties of the actual laminates. Since the thicknesses of the layers in each part were very small in relation to the size of the section, this assumption does not introduce

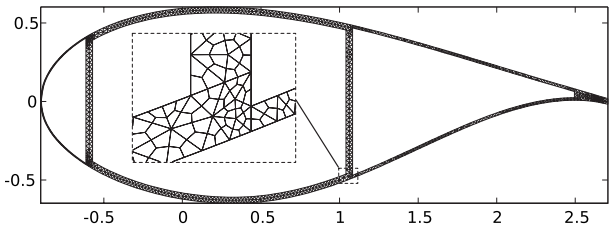

Fig. 4 Example of triangulation for the DU 00-W2-401 airfoil section located at 18% of the blade-span. A detailed view of the triquadrilateral mesh is also shown in the inset.

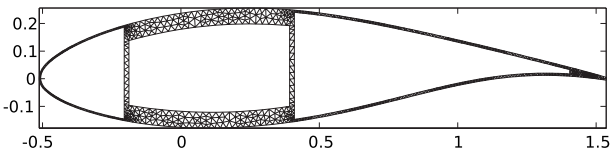

Fig. 5 Example of triangulation for the DU 93-W-210 airfoil section located at 60% of the blade-span

Table 2 List of the first three frequencies for the validation test: comparison of the Myklestad method against the method presented in this work

Mode	Myklestad (Hz)	Present work (Hz)
first flapwise	0.5793	0.9307
first chordwise	1.058	1.426
second flapwise	2.320	2.298

a significant error. Besides, if more detail is required, our code allows for independent meshing of every single layer of material separately using the exact properties.

In order to provide an order-of-magnitude verification, we ran a set of comparisons against a linear Timoshenko beam model [24,25], to test the static response of our model, and the Myklestad method, to test the dynamics. As the Myklestad method cannot consider twisted beams, we used a blade with the same representative sections but untwisted. Regarding the static part, we compared results for the blade tip deflection in two load situations. For the case of a uniformly chord-normal loaded blade with a distributed load of 1000 N/m, our model predicted a deflection of 0.835 m while Timoshenko's model predicted a deflection of 0.704 m. Since our model also takes into account couplings between different deformation modes, it also gave a nonzero chordwise deflection of 0.014 m, which was not predicted by Timoshenko's model. For the case of the aerodynamic load distribution at the steady state, our model predicted a chord-normal deflection of 3.566 m compared with 3.012 m predicted by the Timoshenko classic theory, with a chordwise deflection of 0.286 m against 0.092 m. The reported 20% difference in the main (chord-normal) component of the blade tip deflection is clearly what it may be expected from this sort of order-of-magnitude comparison. Concerning the differences in the chordwise deflection, the crosslink between the two bending modes in the generalized Timoshenko (which is completely absent in the classical Timoshenko theory) is likely to affect substantially the value of the comparatively smaller chordwise deformation. The Myklestad method is used as a first-approach way to obtain the characteristic bending frequencies of a beam, so it is a good candidate to test the accuracy of our model to predict the dynamics of the blade. It represents the beam as a collection of concentrated masses distributed along a weightless beam with bending stiffness corresponding to that the actual one [26]. Table 2 shows the two first flap- and chordwise bending frequencies obtained from both methods. The difference between the results of each method can be attributed to the fact that our method takes into account couplings between strain measures that give rise to combined deformation modes, and the Myklestad method is constructed on the assumption that all the modes are purely flexural. It is interesting to note that in this case, where the blade is untwisted, the couplings arise only from asymmetries in the section shape and material distribution.

After this verification, we turn into the calculation of the steady state of the twisted blade under nominal loading conditions. The aerodynamic loads for these tests were computed using the blade-element momentum model described in chapter 3 of Ref. [26], which was also used for the basic aerodynamic design of the blade geometry. In this set of experiments for the steady-state calculations we assumed a nominal wind speed $W_\infty = 11$ m/s and a tip-speed ratio $\lambda = 7$, which resulted in the rotor's angular speed $\omega = 1.86$ rad/s. These values were applied as boundary conditions for the 1D model, which automatically incorporates the effects of the centrifugal loads into solution.

Figure 6 shows the displacement of the reference line U when the beam is subjected to a steady load in normal operational conditions, and Fig. 7 shows the corresponding rotations of the beam sections θ. In order to provide a common reference for these two geometrical magnitudes, they were referred to a coordinate system

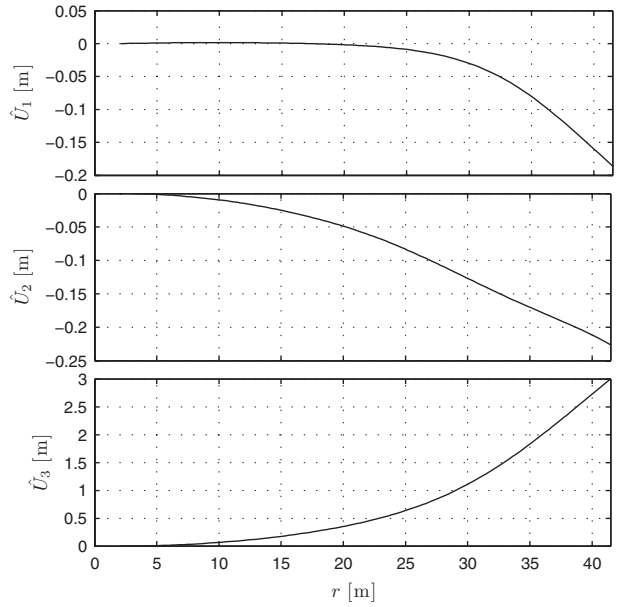

Fig. 6 Displacements of the reference line *U* when the beam is subjected to a steady load in normal operational conditions (referred to a coordinate system aligned with the rotor's plane)

aligned with the rotor's plane, with the first unit vector in the radial direction, the second in the tangential direction pointing to the leading edge, and the third being normal to the rotor's plane.

Next, we solved the eigenvalues problem in Eq. (12) to get the linear modes of vibration around the steady-state configuration computed before, and their corresponding frequencies. Table 3 summarizes the results for the first ten modes, including the frequency and the dominant component of U and θ for each mode. Figure 8 shows the amplitude of the deformation along the span for the three components of U and θ, normalized by the dominant component, for the first three modes.

After computing the global deformation from the 1D beam analysis, we recovered the corresponding 3D fields (displacements, stresses, and strains) using the 3D warping functions previously calculated with VABS. Figure 9 shows the six components of the Jaumann–Biot–Cauchy stress tensor $\mathbf{Z}=\mathcal{S}\boldsymbol{\Gamma}$ for the section located at 60% of the blade-span in the system of coordinates (X^1,X^2,X^3). The dominant stress component $\mathbf{Z}_{11}$ is the one primarily associated with the bending loads, and Fig. 10 shows the plots of $\mathbf{Z}_{11}$ for three other locations along the span, i.e., 25%, 45%, and 95%.

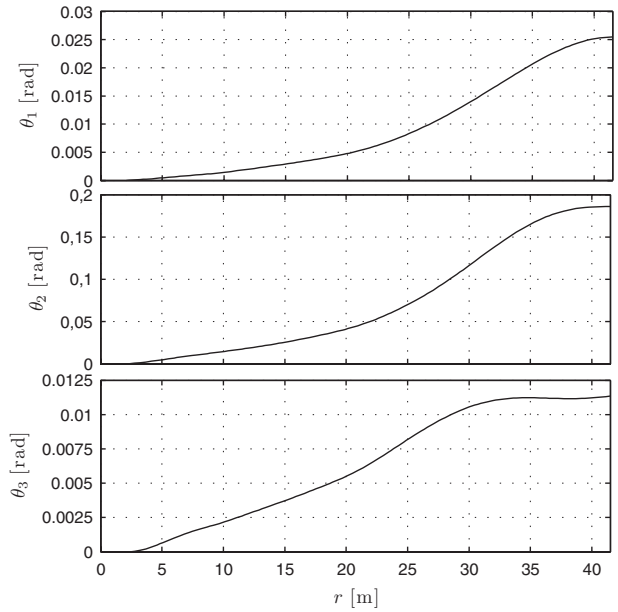

Fig. 7 Rotations of the beam sections θ when the beam is subjected to a steady load in normal operational conditions (referred to a coordinate system aligned with the rotor's plane)

Table 3 List of frequencies and dominant components of *U* and θ for the first ten modes of vibration

Mode	Frequency (Hz)	Dominant U	Dominant θ
1	0.9700	U_3	θ_2
2	1.4167	U_2	θ_3
3	2.3786	U_3	θ_2
4	3.9081	U_2	θ_3
5	5.1708	U_3	θ_2
6	8.6221	U_3	θ_2
7	9.4012	U_3	θ_1
8	11.066	U_2	θ_1
9	11.497	U_3	θ_2
10	13.202	U_3	θ_2

4 Conclusions and Outlook for Further Work

We have introduced an evolution of the VABS approach in which, by the use of the Lagrangian-multiplier technique to constrain the warping rigid modes on the variational formulation, the procedure is simplified and made compatible with internal-node condensation in the triquadrilateral, unstructured finite-element

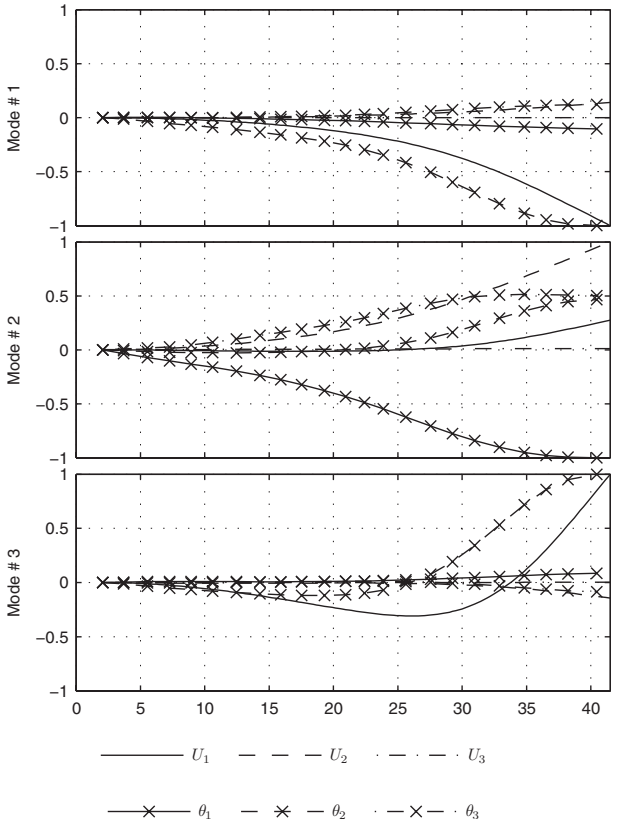

Fig. 8 Amplitudes of *U* and θ for the first three modes of vibration around the steady-state configuration (normalized by the dominant component)

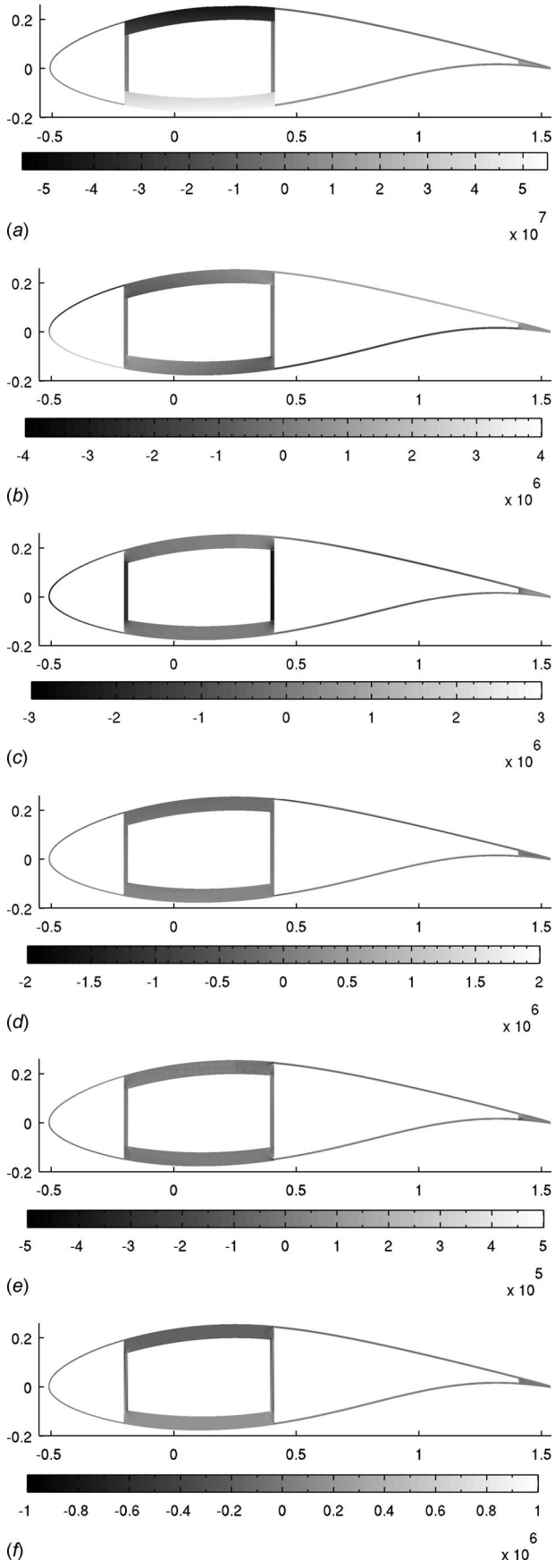

Fig. 9 The six components of the Jaumann–Biot–Cauchy stress tensor $Z=\mathcal{S}\Gamma$ for the section located at 60% of the blade-span (referred to the intrinsic coordinate system (X^1, X^2, X^3))

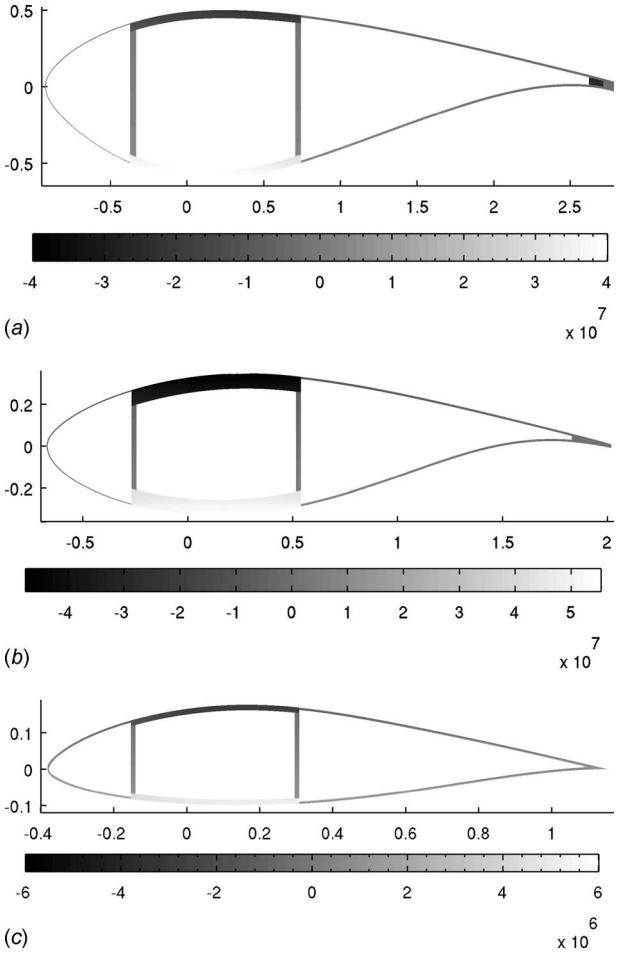

Fig. 10 The dominant stress component Z_{11} for three other locations along the span, i.e., 25%, 45%, and 95% (referred to the intrinsic coordinate system (X^1, X^2, X^3)).

discretization. The method presented in this paper has the advantage of modeling the structural behavior of wind-turbine blades with a one-dimensional model equivalent to the 3D problem in the strain energy sense, which translates into substantial savings in computational cost as the structural problem is solved along many timesteps. The stiffness and inertia matrices are precalculated at the beginning of the computation when the blade geometry is defined. These matrices may be used along the whole simulation of the dynamic problem, and even for several different problems, as long as the blade geometry and structural design remain the same.

Besides being useful for modeling the dynamic response of the beam structure, the one-dimensional model could also be used (as we did in Sec. 3) to compute for a fast, but accurate, solution for the deformed state of the blade when subjected to a steady load in normal operational conditions, and an analysis of the vibrational modes around this steady configuration. This provides a valuable tool to use during the design process. In the adaptive blade concept (see Refs. [27,28], among others), tailoring of the flexo-torsional modes of the blade is used to reduce aerodynamic loads by controlling the coupling between bending and twisting. In that sense, VABS capacity to capture, at least theoretically, the bending-twisting coupled modes in its fully populated 6×6 stiffness matrix for the 1D beam problem would give this model the ability to simulate the dynamic performance of *adaptive blades*.

We plan to continue our work with a dynamic simulation of the fluid-structure problem. In a first stage, we plan to couple the phenomena by feeding back changes in the geometry due to blade

deformation in our basic aerodynamic model and recomputing the forces. At this stage, we also plan to include statistically generated perturbations to represent fluctuations in wind speed and direction based on anemometry data for wind resource in several representative locations.

Besides providing us with a fast tool for a quick analysis, the model presented here will serve as an intermediate step before the ultimate goal of coupling the structural response with an advanced nonlinear adaptive model of the unsteady flow, called the KLE model [29,15], which is based on the vorticity-velocity formulation of the Navier–Stokes equations. We believe that this combination would have the potential of offering performance advantages over the present fluid-structure solvers.

Acknowledgment

We would like to acknowledge the financial support made available by the U.S. Air Force Office of Scientific Research through Grant No. FA9550-06-1-0516. We are also very grateful to Professor W. A. Timmer from Delft University, The Netherlands, who kindly provided detailed data on the aerodynamic performance and geometrical construction of the DU airfoil series.

References

[1] de Vries, E., 2005, "Thinking Bigger: Are There Limits to Turbine Size?," Renewable Energy World, **8**(3), pp. 42–55.
[2] Hansen, M. O. L., Sørensen, J. N., Vousitas, S., Sørensen, N., and Madsen, H. A., 2006, "State of the Art in Wind Turbine Aerodynamics and Aeroelasticity," Prog. Aerosp. Sci., **42**, pp. 285–330.
[3] Hodges, D. H., Atilgan, A. R., Cesnik, C. E. S., and Fulton, M. V., 1992, "On a Simplified Strain Energy Function for Geometrically Nonlinear Behaviour of Anisotropic Beams," Composites Eng., **2**, pp. 513–526.
[4] Yu, W., Hodges, D. H., Volovoi, V., and Cesnik, C. E. S., 2002, "On Timoshenko-Like Modeling of Initially Curved and Twisted Composite Beams," Int. J. Solids Struct., **39**, pp. 5101–5121.
[5] Cesnik, C. E. S., and Hodges, D. H., 1995, "Stiffness Constants for Composite Beams Including Large Initial Twist and Curvature Effects," Appl. Mech. Rev., **48**(11S), pp. S61–S67.
[6] Hodges, D. W., 2006, *Nonlinear Composite Beam Theory*, AIAA, Reston, VA.
[7] Popescu, B., and Hodges, D. H., 2000, "On Asymptotically Correct Timoshenko-Like Anisotropic Beam Theory," Int. J. Solids Struct., **37**, pp. 535–558.
[8] Yu, W., and Hodges, D. H., 2005, "Generalized Timoshenko Theory of the Variational Asymptotic Beam Sectional Analysis," J. Am. Helicopter Soc., **50**, pp. 46–55.
[9] Cesnik, C. E. S., and Hodges, D. H., 1997, "VABS: A New Concept for Composite Rotor Blade Cross-Sectional Modeling," J. Am. Helicopter Soc., **42**, pp. 27–38.
[10] Hodges, D. H., and Yu, W., 2007, "A Rigorous, Engineering-Friendly Approach for Modeling Realistic, Composite Rotor Blades," Wind Energy, **10**, pp. 179–193.
[11] Popescu, B., Hodges, D. H., and Cesnik, C. E. S., 2000, "Obliqueness Effects in Asymptotic Cross-Sectional Analysis of Composite Beams," Comput. Struct., **76**, pp. 533–543.
[12] Berdichevsky, V. L., 1979, "Variational-Asymptotic Method of Constructing a Theory of Shells," J. Appl. Math. Mech., **43**, pp. 664–687.
[13] Cesnik, C. E. S., Sutyrin, V. G., and Hodges, D. H., 1996, "Refined Theory of Composite Beams: The Role of Short-Wavelength Extrapolation," Int. J. Solids Struct., **33**, pp. 1387–1408.
[14] Bathe, K. J., 1996, *Finite Element Procedures*, Prentice Hall, Englewood Cliffs, NJ.
[15] Ponta, F. L., 2006, "The KLE Method: A Velocity-Vorticity Formulation for the Navier–Stokes Equations," ASME J. Appl. Mech., **73**, pp. 1031–1038.
[16] Hodges, D. H., 2003, "Geometrically Exact, Intrinsic Theory for Dynamics of Curved and Twisted Anisotropic Beams," AIAA J., **41**, pp. 1131–1137.
[17] Patil, M. J., and Althoff, M., 2006, "Energy-Consistent, Galerkin Approach for the Nonlinear Dynamics of Beams Using Mixed, Intrinsic Equations," *Proceedings of the AIAA/ASME/ASCE/AHE/ASC Structures, Structural Dynamics and Material Conference*, Reston, VA, pp. 1–9.
[18] Karniadakis, G. E., Bullister, E. T., and Patera, A. T., 1985, "A Spectral Element Method for Solution of Two- and Three-Dimensional Time-Dependent Incompressible Navier–Stokes Equations," *Finite Element Methods for Nonlinear Problems*, Springer-Verlag, New York, p. 803.
[19] Patera, A. T., 1984, "A Spectral Element Method for Fluid Dynamics: Laminar Flow in a Channel Expansion," J. Comput. Phys., **54**, pp. 468–488.
[20] Hodges, D. H., 1990, "A Mixed Variational Formulation Based on Exact Intrinsic Equations for Dynamics of Moving Beams," Int. J. Solids Struct., **26**, pp. 1253–1273.
[21] Timmer, W. A., and van Rooij, R. P. J. O. M., 2003, "Summary of the Delft University Wind Turbine Dedicated Airfoils," *Proceedings of the 41st Aerospace Sciences Meeting and Exhibit*, Reno, NV.
[22] Composites, T. P. I., 2002, "Parametric Study for Large Wind Turbine Blades-,"Sandia National Laboratories, Report No. SAND2002-2519.
[23] Griffin, D. A., 2002, "Blade System Design Studies Volume I: Composite Technologies for Large Wind Turbine Blades," Sandia National Laboratories, Report No. SAND2002-1879.
[24] Otero, A. D., and Ponta, F. L., 2004, "Finite Element Structural Study of the VGOT Wind Turbine," Int. J. Global Energy Issues, **21**, pp. 221–235.
[25] Otero, A. D., and Ponta, F. L., 2009, "On the Structural Behaviour of Variable-Geometry Oval-Trajectory Darrieus Wind Turbines," Renewable Energy, **34**(3), pp. 827–832.
[26] Manwell, J. F., McGowan, J. G., and Rogers, A. L., 2002, *Wind Energy Explained: Theory, Design and Application*, Wiley, Chichester, UK.10.1002/0470846127
[27] Griffin, D. A., 2002, "Evaluation of Design Concepts for Adaptive Wind Turbine Blades," Sandia National Laboratories, Report No. SAND2002-2424.
[28] Locke, J., and Contreras Hidalgo, I., 2002, "The Implementation of Braided Composite Materials in the Design of a Bend-Twist Coupled Blade," Sandia National Laboratories, Report No. SAND2002-2425.
[29] Ponta, F. L., 2005, "The Kinematic Laplacian Equation Method," J. Comput. Phys., **207**, pp. 405–426.